

Squeeze Film Damper Suppression of Thermal Bow-Morton Effect Instability

Dongil Shin

Department of Mechanical Engineering,
Texas A&M University,
College Station, TX 77840
e-mail: davshin@tamu.edu

Alan B. Palazzolo¹

Professor
Fellow ASME
Department of Mechanical Engineering,
Texas A&M University,
College Station, TX 77840
e-mail: a-palazzolo@tamu.edu

Xiaomeng Tong

Mem. ASME
Department of Mechanical Engineering,
Texas A&M University,
College Station, TX 77840
e-mail: tongxiaomeng1989@tamu.edu

The Morton effect (ME) is a synchronous vibration problem in turbomachinery caused by the nonuniform viscous heating around the journal circumference, and its resultant thermal bow (TB) and ensuing synchronous vibration. This paper treats the unconventional application of the SFD for the mitigation of ME-induced vibration. Installing a properly designed squeeze film damper (SFD) may change the rotor's critical speed location, damping, and deflection shape, and thereby suppress the vibration caused by the ME. The effectiveness of the SFD on suppressing the ME is tested via linear and nonlinear simulation studies employing a three-dimensional (3D) thermohydrodynamic (THD) tilting pad journal bearing (TJPB), and a flexible, Euler beam rotor model. The example rotor model is for a compressor that experimentally exhibited an unacceptable vibration level along with significant journal differential heating near 8000 rpm. The SFD model includes fluid inertia and is installed on the nondrive end bearing location where the asymmetric viscous heating of the journal is highest. The influence of SFD cage stiffness is evaluated. [DOI: 10.1115/1.4048602]

Introduction

Synchronous orbiting of a journal induces differential heating around the journal circumference, on a shaft supported by hydrodynamic bearings. The asymmetric heating may lead to a thermal bow (TB), which causes an increased inertial (imbalance) force applied to the system. This excitation will produce an increased vibration level and subsequently more asymmetric differential heating, which was the cause of the thermal bow. The positive feedback formed by the differential journal heating, the bow, and the vibration may drive the rotor to a condition with unacceptable vibration levels, and this phenomenon is referred to as the Morton effect (ME). The ME has been more frequently observed in the modern turbomachinery with an increasing demand for high-speed and load operation [1,2].

De-Jongh and Hoeven [3] observed ME instability in an overhung rotor, which showed a high vibration level caused by journal differential heating. Keogh and Morton [4] developed a simple analysis model with short bearing theory and an isoviscous model to investigate the ME. Lee and Palazzolo [5] employed a finite element method (FEM) to develop a multiphysics model incorporating a variable viscosity Reynolds and energy equations. Suh and Palazzolo [6–9] and Tong et al. [10–13] advanced the ME prediction model with a three-dimensional (3D) thermoelastohydrodynamic tilting pad journal bearing (TPJB), distributed thermal bow and a double overhung rotor configuration, and the application of the ME to gas journal bearings. Tong and Palazzolo [14] built a test rig to measure the journal differential heating and validated the accuracy of the high-fidelity ME prediction model in Refs. [10–13] by comparing it with measured journal temperatures.

Squeeze film dampers (SFD) are widely used to enhance the stability of a rotor-bearing system and suppress vibration by providing viscous damping. Leader et al. [15] and Edney and Nicholas [16] examined steam turbines experiencing high synchronous vibration and mitigated the vibration utilizing SFD in series with TPJBs. Kanki et al. [17] investigated a steam turbine exhibiting subsynchronous vibration and overcame the instability by installing SFD at the bearing. Ferraro et al. [18] and Ertas et al. [19]

adopted an integral SFD (ISFD) to suppress the subsynchronous vibration of steam turbines. The ISFD alleviated the vibration and provided stable operation of the rotor.

The effects of SFD parameters such as damping properties and cage stiffness on the rotor vibration were presented in the literature. Gunter et al. [20] demonstrated an optimum damping value for rotor-bearing systems, which depends on the rotor's stiffness ratio between the bearing support and the shaft bending stiffness. Chu and Homes [21] examined the effect of cage stiffness and SFD damping on the location of the critical speed and vibration level, both theoretically and experimentally.

The SFD is commonly equipped with a supply groove for sufficient lubricant flow into the film gap. The added mass induced by the groove has a substantial influence on the dynamic response of a grooved SFD and has been analyzed extensively [22–24]. The force coefficients of SFD with a central groove were experimentally verified in Refs. [25–28]. Delgado and San Andres [29,30] presented a linear fluid inertia bulk flow model for the analysis of the centrally grooved SFD. An effective clearance ratio was adopted based on the measured data from the test rig to replace the actual groove clearance. Linear analysis, which uses linearized stiffness and damping coefficients, maintains its accuracy when the shaft whirling motion is relatively small.

Retrofitting of an existing bearing to install a SFD would depend on the original bearing support structure. Quite often, the bearing housing is cylindrical in shape and slides into a mating hole in the machinery casing. The hole may be split or continuous depending on the design of the machine. Installation of the SFD would then require increasing the bore diameter of the hole to provide for the oil gap of the SFD. In addition, modifications for sealing the SFD with O-rings or by another means or collecting the oil in the case of an open-ended SFD, would be required. This approach will minimize the need for a larger envelope for the bearing modified to include the SFD.

Simulation of a rotor-journal bearing system under a high dynamic loading condition requires a nonlinear simulation for accurate prediction. Bonello et al. [31] studied the interaction between the SFD and flexible rotor based on a harmonic balance method and found that the cavitation effect increases with higher static eccentricity of the SFD and affects the damping capability of the SFD. He [32] utilized an improved harmonic balance method to analyze the flexible rotor with a SFD. Cao et al. [33] simulated the nonlinear short SFD model in series with a fluid

¹Corresponding author.

Manuscript received August 25, 2020; final manuscript received September 3, 2020; published online December 1, 2020. Editor: Jerzy T. Sawicki.

film bearing and applied this to a coupled lateral–torsional rotor system. The nonlinear time transient solutions were obtained via the Runge–Kutta method.

Measures to suppress the ME vibration have been limited to changing rotor-bearing parameters such as bearing radial clearance, bearing length, overhung mass, etc. To the best of our knowledge, there has not been any published study regarding the potential of SFD for suppressing the ME. This paper presents a computational study of the ME instability and its suppression by including the SFD in series with a TPJB. A linear response study was conducted in order to provide conventional rotordynamic response as part of a complete description of the example rotor system. Simulated results demonstrate that installing a properly designed squeeze film damper shifts the critical speed and alters the deflection shape of a rotor, which may help attenuate the ME vibration. The present work employs a finite element-based SFD model including the inertia effect from a central groove [34], which is similar to the linear bulk-flow model in Refs. [29] and [30]. The multiphysics ME simulation model includes 3D thermo-hydrodynamic (THD) models of the fluid film, and 3D solid FEM bearing and journal thermal and structural models and flexible shaft dynamics models as similar to [35,36]. Both linear and nonlinear transient simulations are performed to compare the rotor dynamic performances and journal temperature differential with and without the SFD. The linear analysis confirms the shift of critical speed, damping ratio, and the modified mode shape due to the SFD. Optimal parameters of SFD are developed that substantially attenuate the ME vibration in nonlinear simulations.

Modeling and Morton Effect Prediction Algorithms

Centrally Grooved Squeeze Film Damper. The Reynolds equation (RE) for an incompressible lubricant is employed to obtain the fluid pressure distribution in the SFD film. The RE combines the momentum and fluid continuity equations into the partial differential equation

$$\frac{\partial}{\partial \theta_D} \left(\frac{h_D^3}{12\mu_D} \frac{\partial p}{\partial \theta_D} \right) + \frac{\partial}{\partial z} \left(\frac{h_D^3}{12\mu_D} \frac{\partial p}{\partial z} \right) = \frac{R_J \omega_J}{2} \frac{\partial h_D}{\partial \theta_D} + \frac{\partial h_D}{\partial t} \quad (1)$$

where R_J and μ_D denote the radius of the SFD journal and the viscosity of the lubricant, respectively. The term $\frac{R_J \omega_J}{2} \frac{\partial h_D}{\partial \theta_D}$ is set to zero for the force calculation of the SFD since its bearing housing is normally fixed in the circumferential direction with an antirotation pin or a cage to prevent the bearing housing rotation. In Fig. 1, x_J and y_J are the bearing housing center displacement with respect to the SFD center O_D .

The film thickness of the fluid and its derivative are expressed as

$$\begin{aligned} h_D(\theta_D) &= C_D - x_J \cos \theta_D - y_J \sin \theta_D \\ \frac{\partial h_D(\theta_D)}{\partial t} &= -\dot{x}_J \cos \theta_D - \dot{y}_J \sin \theta_D \end{aligned} \quad (2)$$

where C_D represents the SFD radial clearance and θ_D denotes the circumferential coordinate of the SFD lubricant.

The finite element level form of the Reynolds equation is represented as

$$K_E P_E = S_E + I_E \quad (3)$$

where $(K_E)_{ik} = \left(\frac{h_{DE}^3}{12\mu} \right) \int_{\Omega} \left(\frac{\partial N_i}{\partial x} \frac{\partial N_k}{\partial x} + \frac{\partial N_i}{\partial y} \frac{\partial N_k}{\partial y} \right) dx dy$ and $i, k = 1, 2, 3$. The damping source term is $(S_E)_i = (h_{DE}/\partial t) \int_{\Omega} N_i dx dy$, and the fluid inertia term is $(I_E)_i = \left(\frac{\rho_D h_{DE}^2}{12\mu} \frac{\partial^2 h_{DE}}{\partial t^2} \right) \int_{\Omega} N_i dx dy$.

Triangular simplex finite elements interpolate the two-dimensional film pressure distribution and are expressed with shape functions and node pressure vectors as

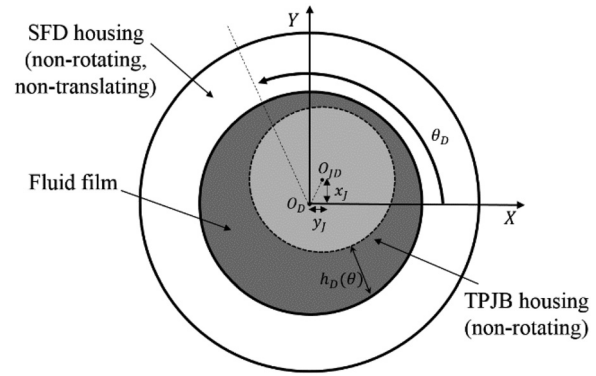


Fig. 1 Axial midplane of SFD

$$\begin{aligned} p(x, y) &= N^T P_E \\ N^T &= (N_1, N_2, N_3) \\ P_E^T &= (P_{1E}, P_{2E}, P_{3E}) \end{aligned} \quad (4)$$

Values obtained from the current model are compared in Fig. 2 with results from Ref. [29], which are based on a linear bulk flow model. The schematic showing the series combination of the journal, tilting pads, TPJB housing, SFD film, and outer SFD housing is shown in Fig. 3. The groove geometry of the SFD including the inlet groove depth (d_I) and film clearance (C_D) used in Fig. 2 is also illustrated in the figure. The SFD parameter values, including the pressure boundary conditions, inlet/outlet groove length, and effective groove/film clearance from Ref. [29] are applied to the current model. The compared result shows good agreement between the two models.

The instantaneous reaction force applied to the bearing housing is obtained by integrating the pressure distribution. Considering the half symmetry of the lubricant, the bearing housing reaction force becomes

$$F_D = \begin{Bmatrix} F_{Dx} \\ F_{Dy} \end{Bmatrix} = 2 \int_0^{L/2} \int_{-\pi}^{\pi} p \begin{Bmatrix} \cos \theta_D \\ \sin \theta_D \end{Bmatrix} d\theta_D dz_D \quad (5)$$

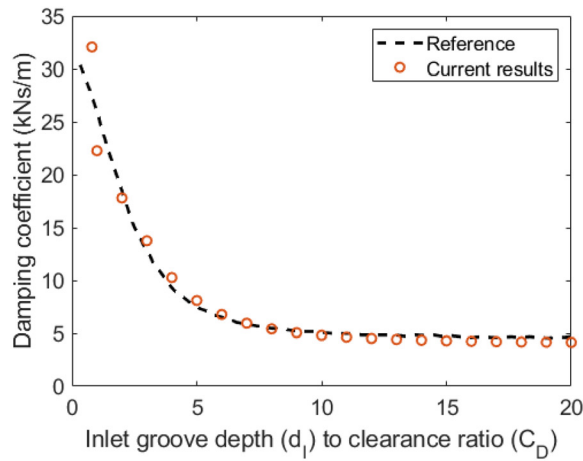
Note that the lubricant temperature variation of the SFD is assumed negligible in the example rotor system because the SFD is prevented from rotation with a cage. In addition, the initial SFD lubricant temperature is assumed to be the same as the TPJB supply oil temperature, and therefore temperature change in the SFD lubricant caused by the supply oil and thermal structures of SFD/TPJB housings are not considered in this study.

Tilting Pad Journal Bearing Model. Accurate prediction of the ME phenomenon requires a high-fidelity THD TPJB model. The generalized Reynolds equation for an incompressible fluid with variable lubricant viscosity and negligible fluid inertia/shaft curvature is employed [6,7]. The temperature-dependent variable viscosity is obtained from the calculated film temperature distribution and the viscosity–temperature relation

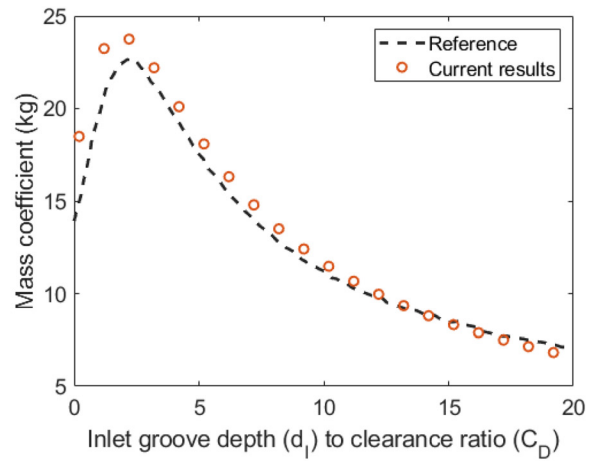
$$\mu = \mu_0 e^{-\alpha(T-T_0)} \quad (6)$$

where μ_0 , T_0 , and α are the reference viscosity, film temperature, and the viscosity coefficient, respectively, and the film temperature T is obtained by solving the energy equation.

A cylindrical pivot with angular pad tilting and pivot translational motions are included in the current analysis. The film thickness formula for the cylindrical pivot is



(a)



(b)

Fig. 2 Comparison of (a) damping and (b) added mass coefficient with Ref. [29]

$$\begin{aligned}
 h(\theta, z) = & C_p - \hat{e}_x \cos(\theta) - \hat{e}_y \sin(\theta) \\
 & - (C_p - C_b) \cos(\theta - \theta_p) - \delta_{\text{tilt}} R \sin(\theta - \theta_p) \\
 & - h_{\text{shaft.TE}}(\theta, z) - h_{\text{pad.TE}}(\theta, z)
 \end{aligned} \quad (7)$$

where

$$\hat{e}_x = e_x - y_{\text{pvt}} \cos \theta_p, \quad \hat{e}_y = e_y - y_{\text{pvt}} \sin \theta_p.$$

and C_p , C_b , z , R , θ , and θ_p represent pad and bearing radial clearance, film's axial coordinate, journal radius, bearing circumferential coordinate and pad pivot position, respectively. Note that the film thickness formula considers the asymmetric thermal expansion of the journal ($h_{\text{shaft.TE}}$) and pad ($h_{\text{pad.TE}}$) and pivot deformation caused by the load on pads.

The dynamic equations of the cylindrical pivot TPJB pads are

$$\begin{aligned}
 M_{\text{pad}}^i \ddot{y}_{\text{pvt}} &= -K_p y_{\text{pvt}} + F_{\text{pad}}^i \\
 I_{\text{tilt}}^i \ddot{\delta}_{\text{tilt}} &= N_{\text{tilt}}^i
 \end{aligned} \quad (8)$$

where i denotes the pad number, and M_{pad}^i , I_{tilt}^i , F_{pad}^i , and N_{tilt}^i are the mass and the tilting inertia of a pad, the fluid film force and the tilting moments applied to a pad, respectively.

Thermal Models. The energy equation to calculate the 3D temperature distribution T across the fluid film is

$$\begin{aligned}
 \rho c \left(u \frac{\partial T}{\partial x} + w \frac{\partial T}{\partial z} \right) &= k \left(\frac{\partial^2 T}{\partial x^2} + \frac{\partial^2 T}{\partial y^2} + \frac{\partial^2 T}{\partial z^2} \right) \\
 &+ \mu \left[\left(\frac{\partial u}{\partial y} \right)^2 + \left(\frac{\partial w}{\partial y} \right)^2 \right]
 \end{aligned} \quad (9)$$

where ρ , c , k , u , w are density, specific heat capacity, thermal conductivity, circumferential, and axial velocities, respectively. Equation (9) is solved using 3D, eight-node isoparametric finite elements along with an up-winding scheme [8,9] to prevent spatial oscillations from the convective term.

The Laplace equation is solved using 3D eight-node isoparametric finite elements to predict the temperature distributions of the journal and pads, and its discrete form is

$$[C][\dot{T}] + [K][T] = [F] \quad (10)$$

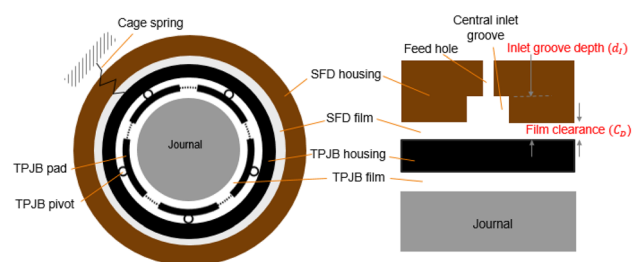


Fig. 3 Schematics of series combination of TPJB and SFD and SFD groove geometry (not to scale)

where F is time-varying thermal load updated with the thermal solutions of the rotor-bearing system. The time-transient solution of Eq. (10) is obtained via numerical integration [8,9]. The heat conduction of the tilting pads and shaft are considered to calculate the pad and shaft temperature distributions. The transient simulation is conducted with the FE model of the pads and shaft including their thermal masses, and with convection boundary conditions applied as explained in Fig. 4.

Accurate prediction of the thermal bow amplitude and its phase is critical to accurately determine ME occurrences. The hybrid beam-solid method used in Ref. [10] is adopted to determine the deformations resulting from the differential heating in the journal while using the computational efficiency of beam finite elements. The calculated thermal bow in the rotating reference frame is converted into the dynamic excitation in the inertial frame equations of motion.

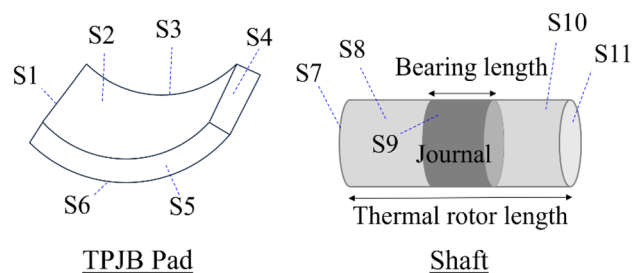


Fig. 4 Thermal boundary conditions on TPJB pads and shaft outer surfaces

Thermal boundary conditions are imposed on the two interfaces (fluid-pad and journal-fluid), pad surfaces, and four outer surfaces of the shaft exposed to atmosphere, as shown in Fig. 4. Temperature boundary conditions are applied to the two interfaces. Note that the thermal conditions need to be applied in the rotating frame for the journal surface mesh, and it is continuously re-oriented in the transient simulation. Table 1 indicates the thermal boundary conditions applied to the surfaces of TPJB pad and shaft. The convection coefficient of 50 W/m²K is used for all the surfaces contacting supply oil (supply oil temperature of 50 °C) and 30 W/m²K is used for all the surfaces in contact with air (room temperature of 30 °C). Note that a convective boundary condition with supply oil temperature of 50 °C is applied to the back of the tilting pads. The model for the pad inlet boundary temperature is adopted from mixing theory in Refs. [6] and [7]. The axial length of the solid and thermal finite element models is seven times the journal length. This specific length is determined from the simulation that induces a negligible change in temperature calculated by the much longer length of the finite element model.

Flexible Rotor With Squeeze Film Damper in Series With a Tilting Pad Journal Bearing. The rotor configuration with a single overhung mass at the nondrive side (NDE) is shown in Fig. 5.

The flexible, lateral rotordynamics, Euler beam-based model of the rotating assembly is represented as

$$[\dot{U}] = [D][U] + [F] \quad (11)$$

where $[U] = \begin{bmatrix} \dot{Z} \\ Z \end{bmatrix}$, $[D] = \begin{bmatrix} -M_{ro}^{-1}C_{ro} & -M_{ro}^{-1}K_{ro} \\ 1 & 0 \end{bmatrix}$, $[F] = \begin{bmatrix} M_{ro}^{-1}F_{ro} \\ 0 \end{bmatrix}$. U , M_{ro} , C_{ro} and K_{ro} are the state variable vector and mass/damping/stiffness matrices of the system, F_{ro} is the force vector including gravity, fluidic forces $F_{B,x,y}$ from the TPJB, imbalance excitation, and dynamic forces induced by thermal bow. This equation is diagonalized using the right and left eigenvectors and modal reduction. For computational economy, only the modes having frequencies below five times the running speed were employed in the simulation.

The SFD dynamic model including the TPJB housing mass, cage spring stiffness, and nonlinear SFD force is included as

$$\begin{bmatrix} M_D & 0 \\ 0 & M_D \end{bmatrix} \begin{bmatrix} \ddot{x}_D \\ \ddot{y}_D \end{bmatrix} = - \begin{bmatrix} K_{Dx} & 0 \\ 0 & K_{Dy} \end{bmatrix} \begin{bmatrix} x_D \\ y_D \end{bmatrix} + \begin{bmatrix} F_{Dx} + M_{Dx} - F_{Bx} \\ F_{Dy} + M_{Dy} - F_{By} \end{bmatrix} \quad (12)$$

where x_D and y_D denotes the x and y displacements of the TPJB housing. M_D , K_{Dx} , K_{Dy} , $F_{D,x,y}$, $F_{B,x,y}$, M_{Dx} , and M_{Dy} represent the TPJB housing mass, cage stiffness in x and y directions, and the transient SFD damping/added mass force and transient TPJB force in the x and y directions. Note that the TPJB force $F_{B,x,y}$ is the sum of each pad force F_{pad}^i in Eq. (8).

The coupling between the TPJB and SFD models was achieved by subtracting the TPJB housing displacement x_D and y_D from the journal displacement of the TPJB in Eq. (11), and incorporating

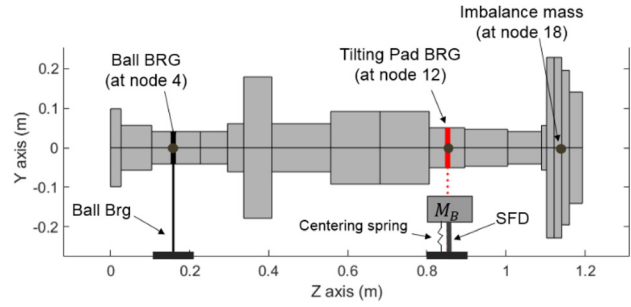


Fig. 5 Example rotor-bearing-SFD configuration

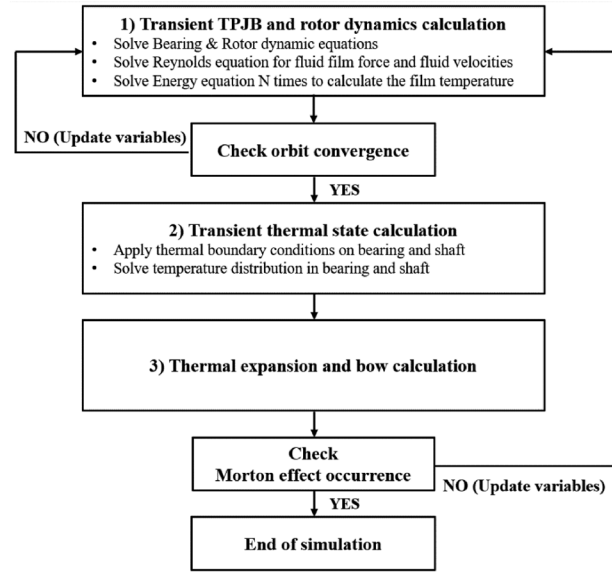


Fig. 6 ME prediction algorithm

the TPJB force $F_{B,x,y}$ into Eq. (12). The whole rotor-bearing-SFD model consists of the TPJB dynamic equation Eq. (8), flexible rotor dynamic equation Eq. (11), and the SFD dynamic equation Eq. (12). The lowest 20 modes of the rotor are retained and used for numerical integration. The three dynamic equations are coupled with each other and solved simultaneously to investigate the SFD effect on the ME suppression.

Morton Effect Prediction Algorithm. The flow diagram representing the ME prediction algorithm is in Fig. 6. The initial conditions for the rotor-bearing-SFD dynamic states, the temperature distribution of fluid film/shaft-bearing structures, and the initial thermal bow amplitude are specified at the first step. Then the time-transient solution of the rotor-bearing-SFD system is obtained via numerical integration based on Eq. (1), (2), (5)–(8), (11), and (12) until all the rotor orbits decay to steady-state

Table 1 Thermal boundary conditions on pad and shaft

Region	Surface	Description	BC types
9	S1, S4	Lateral ends	Convection with oil at supply oil temperature
	S2	Pad-film interface	Prescribed temperature and heat flux from film surface
	S3, S5	Axial ends	Convection with oil at supply oil temperature
	S6	Radial out	Convection with oil at supply oil temperature
Shaft	S7, S11	Axial ends	Prescribed temperature at room temperature
	S8, S10	Radial surfaces	Convection with air at room temperature
	S9	Journal-film interface	Prescribed temperature and heat flux from film surface

conditions. Convergence is considered to have occurred only after the orbits at all rotor nodes in the model have converged. The energy equation is solved 40 times per each orbit cycle for computational efficiency, and the lubricant viscosity obtained from the previous step is updated at the next step (updated 40 times per one orbit cycle). The number 40 is based on many simulation results, which showed a negligible difference by using a larger number of steps. Transient thermal states of the bearing-shaft structures are calculated based on Eqs. (9) and (10), after the orbit convergence is ensured. A staggered-time-integration technique is employed [8,9] for faster simulation, without deteriorating accuracy, since the thermal and vibration related time constants are greatly different in the rotordynamic model.

The steady-state simulation results presented in the following section are also obtained from the transient simulation method explained above. The simulation initiates from the lowest speed of interest and continues until either dynamic/thermal steady-state or rubbing (induced by the ME) occurs. Then, the process starts again at the next higher speed. The linear method estimates linearized stiffness and damping coefficients of the bearings and incorporates them into the matrix of the Euler beam rotor to formulate the system matrix, and the linear method is used for the calculation of critical speed and unbalance response of the system.

Simulation Results

The rotor configuration with a single overhung mass at the non-drive side (NDE) was shown in Fig. 5. The imbalance mass has a magnitude of 135 g mm and is located at node 18 in the figure. The ball bearing at node 4 has linear stiffness and damping values of 1.7×10^8 N/m and 1×10^5 N s/m, respectively, and these values are assumed invariant with operating speed. The parameters of the TPJB with five pads with a load-on-pad and the SFD at node 12 are given in Table 2. The thermal boundary conditions on the pad and shaft surfaces are also listed in the table. The mesh size of the FEM for the thermal and temperature prediction is selected as $40 \times 7 \times 17$ (circumferential, radial, and axial directions) for shaft, and $15 \times 10 \times 10$ (per one pad) for the Reynolds equation lubricant film and $15 \times 10 \times 10$ (per one pad) for the energy equation solver (pad and film). A convergence test with the current mesh size was conducted with three times the current mesh size, and the results showed good agreement with the presented predictions. The mesh size of the squeeze film is 40×15 (circumferential and axial directions). This size is chosen by gradually increasing the mesh size until the SFD force converges. For the numerical integration of the rotor-bearing-SFD system, the

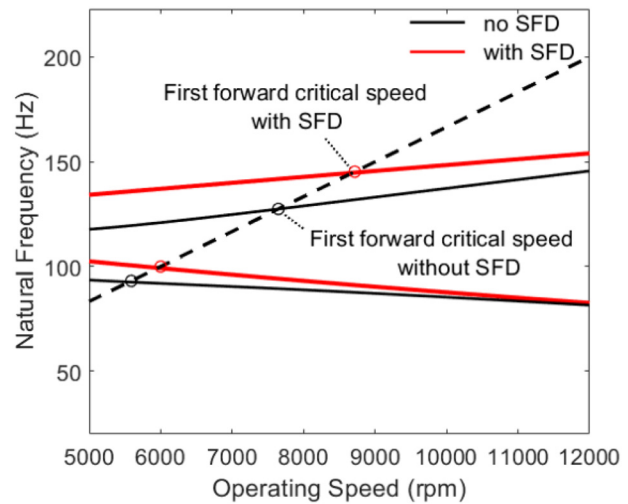


Fig. 7 Campbell diagram of rotors with SFD and without SFD (no SFD indicates rigidly mounted TPJB)

Newmark-beta method is employed with 1000-time steps per one shaft rotation.

Linear Analysis. A linear analysis has been conducted for a more complete description of the example rotor system prior to the nonlinear ME simulation. Note that the method used for the linear analysis is not a linear ME analysis, but a conventional method using linearized dynamic coefficients to calculate the critical speed and unbalance response. Figure 7 shows the Campbell diagram of the rotor-bearing system with and without the SFD using 1×10^8 N/m cage stiffness and nominal parameters in Table 2. The damped first forward critical speed of both cases is found at 7644 rpm for no SFD case and 8708 rpm for with SFD case. It is sometimes noted that the ME occurs mainly when the rotor speed is near the rotor's first bending mode [1,2]. This is not always the case, so care must be exercised to search a far wider speed range when designing to prevent the ME. The ME does occur near the critical speed in the example presented, and an increase in the critical speed may help expand the operating speed range being free from the ME vibration.

The bending mode corresponding to the first forward critical speed without SFD in Fig. 7 is illustrated in Fig. 8.

Table 3 Parameter values for the example system

Lubricant parameters		Bearing parameters	
Viscosity at 50 °C (N s/m ²)	0.0203	Pad type	Load on pad
Viscosity coefficients (1/°C)	0.031	No. pads	5
Supply temperature (°C)	50	Radius of shaft (m)	0.0508
Inlet pressure (Pa)	1.32×10^5	Bearing clearance (μm)	74.9
Reference temperature (°C)	50	Preload	0.5
Shaft parameters		Bearing length(m)	0.0508
Heat capacity (J/kg °C)	453.6	Thermal expansion coefficient (1/°C)	1.3×10^{-5}
Heat conductivity (W/mK)	50	Reference temperature (°C)	25
Thermal expansion coefficient (1/°C)	1.22×10^{-5}	Linear ball bearing	
Reference temperature (°C)	25	K_{xx}, K_{yy} (N/m)	1.7×10^8
Thermal rotor length (m)	0.3508	C_{xx}, C_{yy} (N s/m)	1.0×10^5
SFD parameters		Length (m)	0.0508
TPJB housing mass (kg)	4	Clearance (μm)	100
Diameter (m)	0.15	Fluid density (kg/m ³)	865
Viscosity (Pa · s)	0.03	Effective groove clearance ratio	20
Cage spring stiffness (N/m)	$1 \times 10^8 \sim 8 \times 10^8$	Outlet groove length (m)	0.0041
Inlet groove length (m)	0.0063		

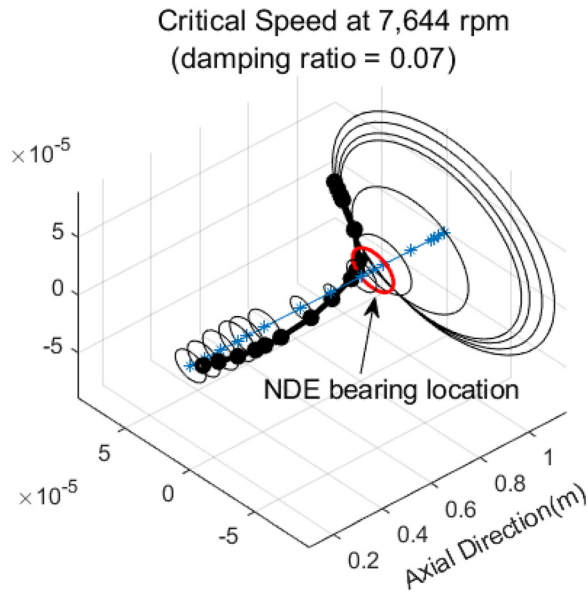


Fig. 8 Bending mode of the example rotor at 7644 rpm

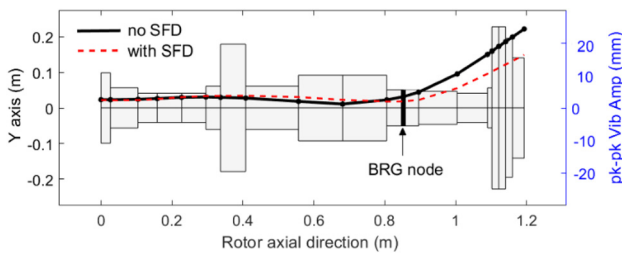


Fig. 9 Distribution of unbalance response amplitudes along the length of the rotor for with and without SFD cases (no SFD indicates rigidly mounted TPJB)

Figure 9 illustrates the deflection shape based on unbalance response of both cases at each critical speed. With the SFD included, the vibration amplitudes at the bearing and the NDE rotor-end nodes have been reduced compared with no SFD case.

In Fig. 10, the SFD cage stiffness values are varied from 1×10^8 N/m to 8×10^8 N/m while other SFD parameters are fixed. The figure illustrates the damped first forward critical speed

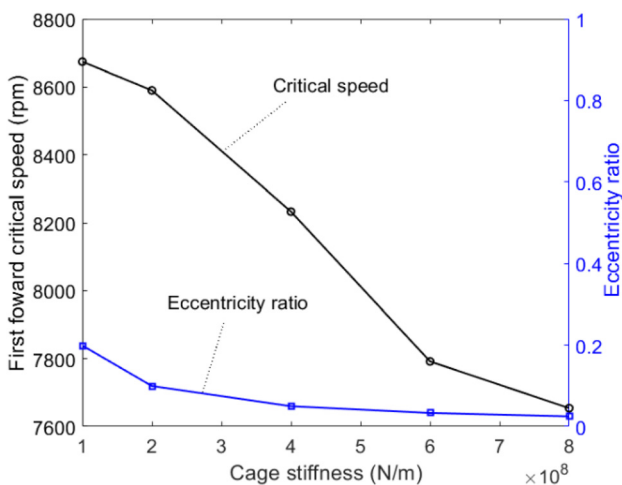


Fig. 10 Linear analysis: damped first forward critical speed and TPJB housing eccentricity ratio

and TPJB housing eccentricities of the SFD with different cage stiffness. The model of the SFD including the cage stiffness assumes that the TPJB bearing housing is centered in the SFD when the bearing load is zero. The bearing load causes the TPJB bearing housing to become slightly eccentric in the SFD when the actual static bearing load is applied. The eccentricity remains very small (<0.2) for all cage stiffness values examined. The SFD damping and inertia coefficients remain nearly constant for this eccentricity range; therefore, the effects of the small eccentricity can be ignored. In the figure, the first forward critical speed shows decreased values with increasing stiffness as opposed to the common conception that high stiffness value leads to an increase in the system's natural frequency.

The trend of decreasing critical speed with higher stiffness is consistent with the observation in Ref. [32]. Note that an increase in the cage stiffness shifts the rotor's critical speed near the critical speed without SFD (7644 rpm) in Fig. 7.

Figure 11 shows the damping ratio and damping coefficient variation with different cage stiffness. The damping ratio increases from the lowest value of 1×10^8 N/m to 4×10^8 N/m and slightly decreases with a further increase to 8×10^8 N/m.

Figure 12 depicts the unbalance responses at the bearing and rotor-end via linear analysis. While the higher vibration level at the NDE rotor-end appears with the lower stiffness in Fig. 12(a), the vibration at the bearing location increases with the stiffer cage in Fig. 12(b).

In Fig. 13, the journal surface ΔT of the rotor with different cage stiffness is presented based on nonlinear transient simulation, which calculates the instantaneous TPJB bearing and SFD forces at each time-step. The thermal bow effect is not included in all cases for comparison purposes. In the figure, an increase in cage stiffness induces more journal ΔT (the journal ΔT is calculated by subtracting the minimum temperature value on the journal surface from the maximum value at the bearing midplane). The results in Fig. 12(b) and 13 imply that for this example, increasing cage stiffness increases the vibration amplitude at the journal, which in turn increases journal ΔT .

This part presents the linear analysis with varying radial clearance and lubricant viscosity of the SFD and investigates the optimal parameters of the SFD in terms of vibration suppression. The nominal parameters in Table 2 and 1×10^8 N/m cage stiffness is used for simulation.

The map in Fig. 14(a) shows a high damping ratio region where the SFD radial clearance ranges from $100 \mu\text{m}$ to $150 \mu\text{m}$. Figure 14(b) shows the corresponding damping coefficient map obtained via identical parameter variation. Note that the highest damping

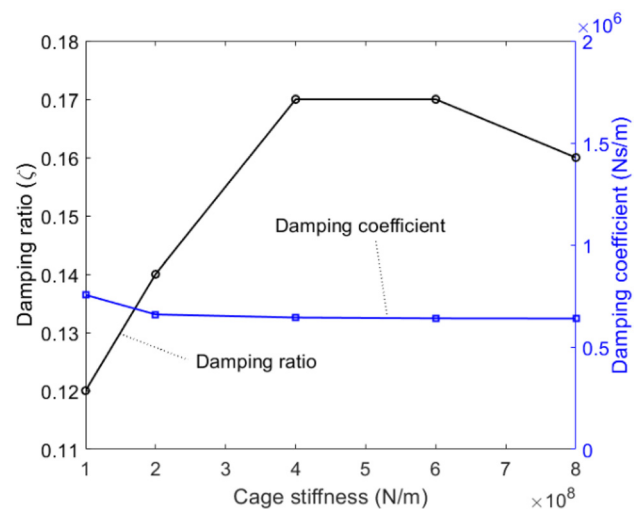


Fig. 11 Linear analysis: damping ratio and damping coefficient change with different SFD cage stiffness

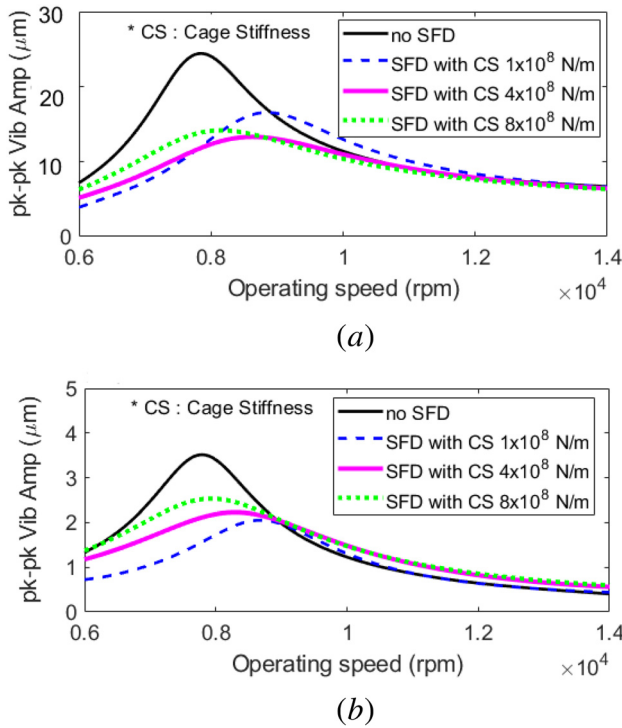


Fig. 12 Linear analysis: unbalance response: (a) pk-pk vibration amplitude at Rotor end node and (b) pk-pk vibration amplitude at bearing node

coefficient of 7.56×10^5 N s/m with 100 μm radial clearance and 0.03 Pa·s lubricant viscosity leads to the lowest damping ratio of 0.11 in Fig. 14(a). The damping coefficient values corresponding to the high damping ratio range from 2×10^5 N s/m to 2.5×10^5 N s/m in Fig. 14(b). Figure 14(c) illustrates the first forward critical speed map with varying parameters. The critical speed shifts up with larger radial clearance, and the highest critical speed reaches up to 13,000 rpm with 300 μm radial clearance. Note that the critical speed is inversely proportional to the damping coefficients as higher critical speeds appear with lower damping coefficients, as indicated in Figs. 14(b) and 14(c). Figure 14(d) shows that SFD radial clearance has a dominant effect on the added mass coefficient variation.

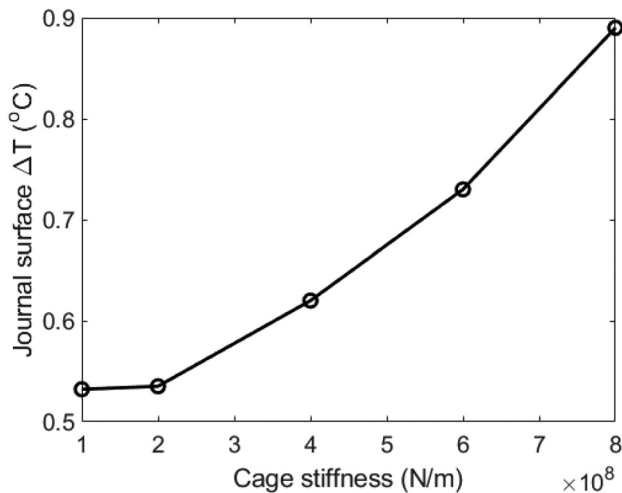


Fig. 13 Nonlinear transient simulation result of journal surface ΔT at steady-state condition with different cage stiffness (without TB effect)

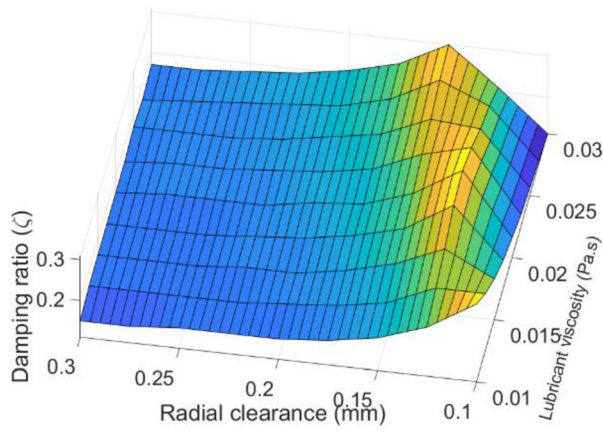
Two parameter sets with high damping ratio (set 1: 0.3 mm radial clearance and 0.015 Pa·s lubricant viscosity and set 2: 0.1 mm radial clearance and 0.01 Pa·s lubricant viscosity) are chosen from the map in Fig. 14(a), and their distribution of unbalance response are drawn in Fig. 15. Both cases show the reduced deflection at the bearing and rotor-end locations than no SFD case. In addition, a significant reduction in the rotor-end deflection is identified compared with the nominal parameter set (0.3 mm radial clearance and 0.01 Pa·s lubricant viscosity).

Nonlinear transient simulation is also performed with two selected sets and the nominal set from 7000 rpm to 10,000 rpm in Fig. 16. Note that the thermal bow effect is not included in all cases for comparison purposes. The two selected cases show decreased vibration level at the TPJB from 7500 rpm to 9,500 rpm compared with the nominal set.

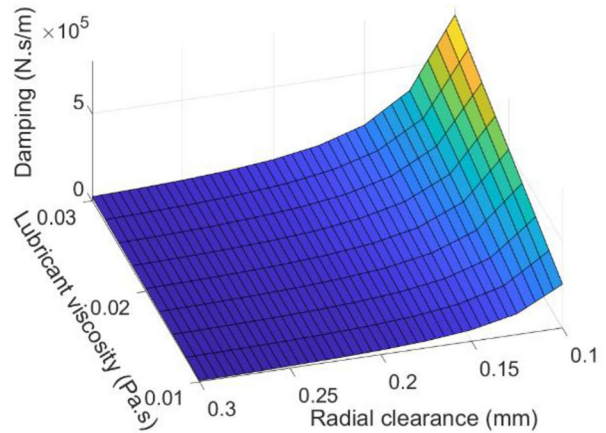
Morton Effect Benchmark Simulation. Morton effect simulations are performed to benchmark the experimentally observed ME case in Ref. [3]. Note that the SFD model is not included in the current analysis, and the parameters of the rotor-bearing configuration are from Table 2. The ME instability phenomenon is identified by observing a substantial increase in vibration caused by including the TB effect, while the vibration amplitudes remain low if the TB effect is not included. More detailed descriptions of the ME instability determination are in Ref. [10]. Note that the exclusion of the TB is achieved by setting the induced thermal bow amplitude to be zero when the dynamic equations of the rotor are solved. Figure 17 illustrates the vibration level of the TPJB at different speeds with and without TB. This result is obtained via the nonlinear steady-state simulation explained in the section Modeling and Morton Effect Prediction Algorithms. The no TB results in the figure are included to show that the large $1 \times$ vibration is caused solely by the ME. The result with TB exhibits much larger vibration amplitude from 8000 rpm to 9000 rpm as compared with the no TB model results. Reference [3] shows high vibrations over a similar speed range. It is notable that the test results in Ref. [3] indicate high vibration as low as 7300 rpm, which is not apparent in the simulation model. This may be due to the effects of pedestal flexibility, lack of precise values of pad-pivot parameters or other unmodeled effects.

Figure 18(a) presents the journal temperature differential ΔT across the rotor axial length at different speeds. The journal ΔT is calculated by subtracting the minimum temperature value on the journal surface from the maximum value at the bearing midplane. Note that only the rotor's axial length from 0.6522 m to 1.0078 m is presented in the figure since the thermal shaft length is designated to be only seven times the bearing length (0.0508 m), as explained in Refs. [8] and [9]. The region where large ΔT appears coincides with the bearing's axial location from 0.8022 m to 0.853 m. The largest ΔT of 28 °C is observed at the bearing midplane near 0.827 m at 8700 rpm, where a rub between the journal and pad surfaces occurs, due to the ME. The large ΔT induces thermal bows with large amplitudes, displacing the overhung disk away from its equilibrium centerline. This causes significant imbalance excitation, which in turn causes high vibration of the rotor. The speed range with large ΔT corresponds to that with high vibration in Fig. 18(b). The high vibration with amplitudes up to 0.15 mm is observed at the rotor axial position from 0.2 m to 0.6 m and the rotor's NDE overhung side (axial length over 1 m). Note that the bending mode of the rotor showed large deflection on the NDE side at 7644 rpm in Fig. 8, which is consistent with the location of the large vibration in the nonlinear simulation results in Fig. 18(b). These results indicate that the ME vibration of the example rotor was closely related to its bending mode at 7644 rpm. The speed range of large vibration is seen to occur above the critical speed and appears from 7800 rpm to 9000 rpm.

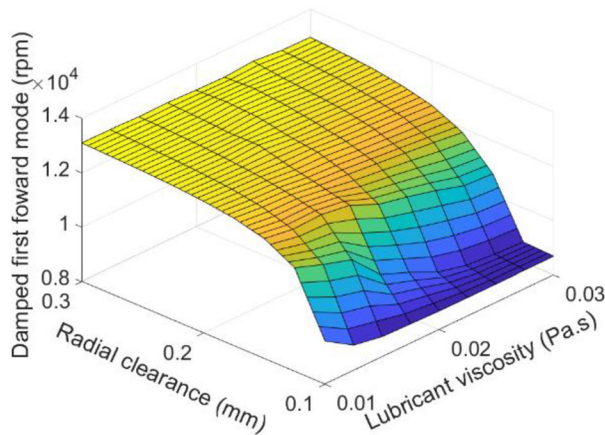
Nonlinear transient simulations are performed both at 8000 and 8500 rpm, and the results are presented in Figs. 19 and 20. All parameter inputs of the system are identical to the aforementioned



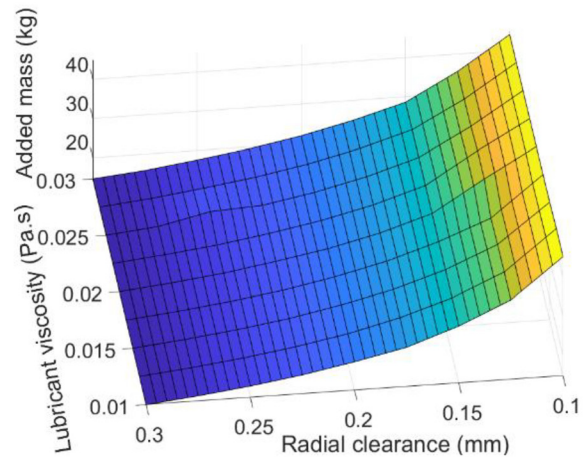
(a)



(b)



(c)



(d)

Fig. 14 Linear analysis with SFD parameter variation (radial clearance and lubricant viscosity): (a) damping ratio of rotor, (b) damping coefficient of SFD, (c) damped first forward critical speed, and (d) added mass coefficient of SFD

nonlinear steady-state simulation, and the SFD is not included. Figure 19 displays a 1X filtered polar plot based on the vibration amplitude and phase at the bearing for both speeds. Note that the texts in the plot denote the simulation time at the instance when the vibration amplitude and phase are plotted. At 8000 rpm, the rotor initially shows a large thermal spiral with time-varying vibration amplitude and phase, which is caused by the large ΔT in Fig. 18(a) and its resultant thermal bow. The vibration amplitude reached its maximum value of 20 μm and then dropped to 2.36 μm

at 25 min, and the phase of the vibration keeps changing from 0 deg to 360 deg during the process. This thermal spiral vibration is the main characteristic of the ME and was experimentally observed in Ref. [3]. At 8500 rpm, a larger thermal spiral with the

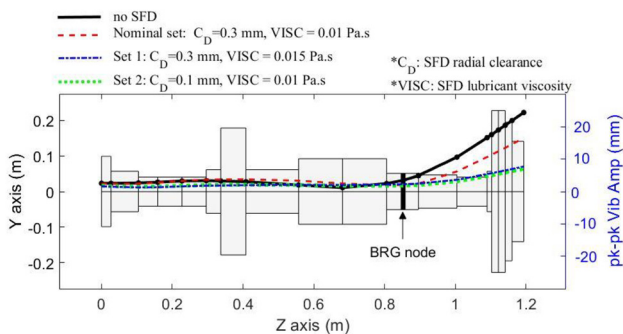


Fig. 15 Distribution of unbalance response amplitudes along the length of the rotor for different SFD parameters (no SFD indicates rigidly mounted TPJB)

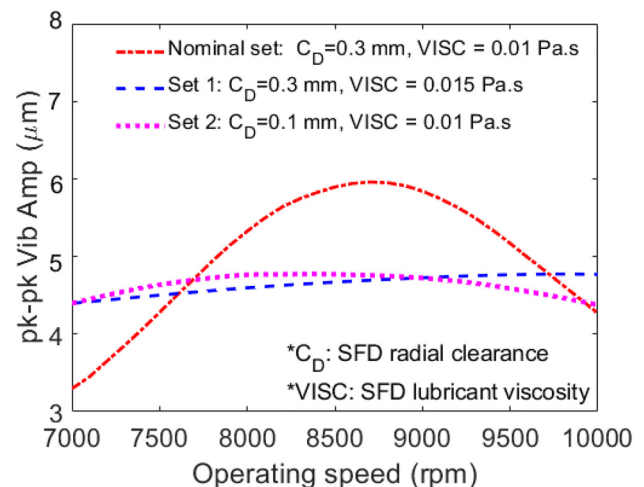


Fig. 16 Nonlinear steady-state simulation: pk-pk vibration amplitude versus rpm at the bearing node with different SFD parameter sets

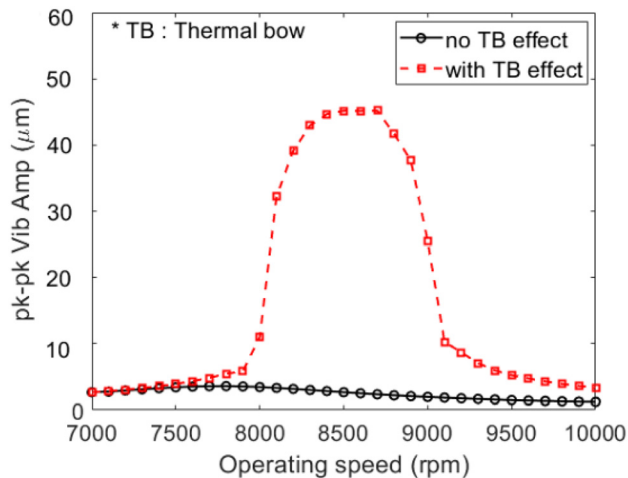


Fig. 17 Nonlinear steady-state simulation: pk-pk vibration amplitude versus rpm at bearing node

maximum amplitude of $25 \mu\text{m}$ appears and does not converge with time.

Although the high vibration level accompanied by time-varying phase, without rub between the journal and pads, is consistent with observations in the experiment in Ref. [3], the predicted vibration levels are lower than the observed ones in Ref. [3]. This may be due to uncertainties in the simulation parameters, including unbalance distribution or other unmodeled effects.

Figure 19 demonstrates that the phase angle migration is more severe at 8500 rpm compared with 8000 rpm. This occurs even though 8500 rpm is displaced further from the linear system model's critical speed at 7644 rpm. This shows that the ME is not strictly a resonance problem. The increase in thermal bow (imbalance) due to the ME at the higher speed dominates over the effect of proximity to the critical speed. This is also reflected in the greater migration of the phase angle at 8500 rpm seen in Fig. 19. Having said this, the disappearance of the ME below 6000 rpm and above 10,000 rpm demonstrates a clear dependency of the ME on proximity to a critical speed.

Figure 20 illustrates the corresponding journal ΔT at the bearing midplane for the rotors with and without TB at two operating speeds. The journal ΔT at 8000 rpm shows a smaller value compared with that of 8500 rpm in most of the simulation, indicating a smaller thermal bow amplitude and less severe vibration at the speed. Note that the temperature oscillations at a fixed location

will depend on the proximity of running speed to the critical speed. If running were well below the critical speed in a region of nonresonant forced response, the hot spot would remain fixed circumferentially. The result without the TB shows stable ΔT converging to around 1°C with time at both speeds. This comparison confirms that the violent vibration in Fig. 19 was induced by the ME. The oscillating amplitude of the ΔT also is consistent with the varying vibration amplitude, as observed in Fig. 19.

Figure 21 illustrates the corresponding temperature distribution at the bearing midplane of the with TB case at 8500 rpm after 25 min. The high journal ΔT of 15.2°C occurs at the hot spot (188.8°) on the journal surface. The high spot denoted with the black rectangular leads the hot spot (192.8°) with 4° . The cold spot is seen at 352.6° , which is 159.8° away from the hot spot.

Effects of Squeeze Film Damper at Different Cage Stiffness. To mitigate the vibration induced by the ME, the SFD model developed is incorporated into the rotor's bearing location, as explained in the section Modeling and Morton Effect Prediction Algorithms. The conventional SFD consists of the cage stiffness and lubricant film at the gap between the TPJB housing and the SFD housing. Reference [21] shows that the proper selection of cage stiffness is crucial for maximizing the damping capability of the SFD.

Figure 22 compares the vibration level at the bearing with different cage stiffness of the SFD. Nonlinear steady-state simulation is carried out from 7000 rpm to 10,000 rpm. Although all stiffness cases display relatively reduced vibration amplitudes compared with the rotor "with TB and without SFD case," they still have higher vibration than when not considering the TB effect. In the figure, the vibration level increases with the stiffer cage, and the $8 \times 10^8 \text{ N/m}$ shows the largest pk-pk vibration amplitude of $28.21 \mu\text{m}$ at 8200 rpm.

Figure 23 displays the $1 \times$ filtered polar plot with different cage stiffness where the results are obtained at each critical speed. The critical speed is defined here as the speed where the maximum pk-pk vibration occurs. In Fig. 22, the maximum pk-pk vibration appears at 8600 rpm for the $1 \times 10^8 \text{ N/m}$ cage stiffness, 8100 rpm for $4 \times 10^8 \text{ N/m}$, and 8200 rpm for $8 \times 10^8 \text{ N/m}$, indicating the shift in critical speed depending on the cage stiffness. Figure 23 shows increasing vibration amplitudes for all three cases, while the operating speed and conditions are kept constant. The amount of vibration increase is more significant with higher stiffness values. The phase angles of the vibration also keep changing during

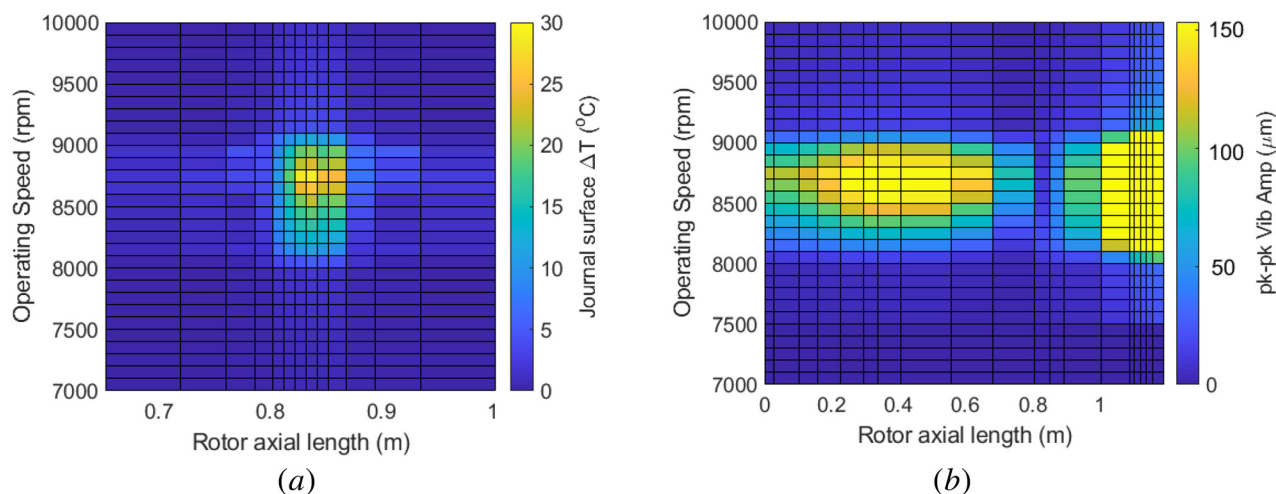


Fig. 18 Nonlinear steady-state simulation: comparison of (a) journal surface ΔT and (b) pk-pk vibration amplitude versus rpm and rotor axial position (with TB effect)

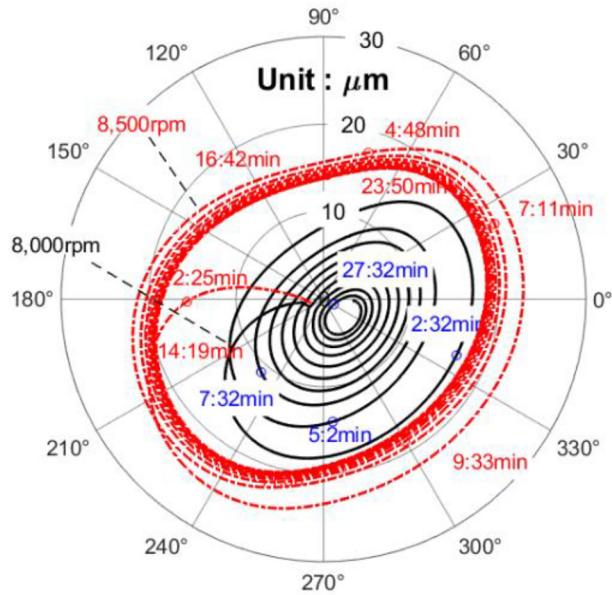


Fig. 19 Nonlinear transient simulation: 1× filtered polar plot at 8000 and 8500 rpm (with TB effect)

the 15 min, but they are not as evident as the rotor without the SFD case in Fig. 19.

Figure 24 shows 3D orbit shapes of the rotor with different cage stiffness obtained via nonlinear simulation. The orbits are drawn at each critical speed after 25 min. In the figure, the orbit sizes of the rotor keep growing and approach the size of the no SFD case with increasing cage stiffness. Note that the orbits with relatively low cage stiffness (1×10^8 N/m) are shifted downward in y direction due to the larger static deflection of the cage.

Figure 25 shows the amplitude of the induced thermal bow corresponding to the result in Fig. 24. In the no SFD case, a large thermal bow amplitude of $27.5 \mu\text{m}$ appears at the rotor end, and its corresponding phase angle is 331 deg, which is 143 deg away from the hot spot in Fig. 21. With the SFD, the thermal bow amplitudes are substantially reduced, as shown in Fig. 25. When the SFD is considered, the most significant thermal bow occurs with the cage stiffness of 8×10^8 N/m, and its value is $18.5 \mu\text{m}$. Relatively small thermal bow amplitudes are induced with low

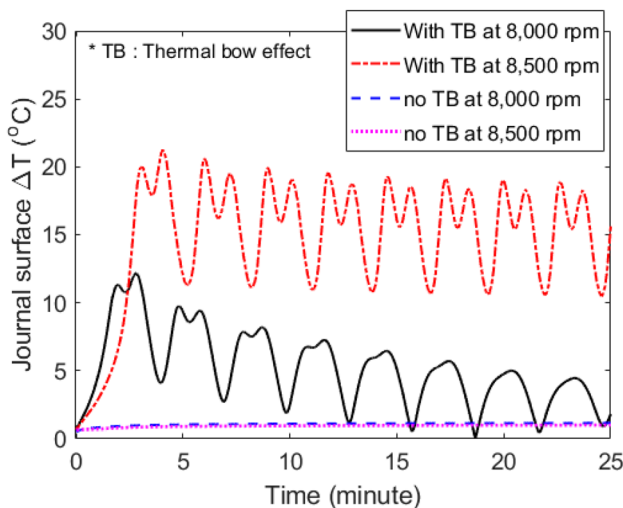


Fig. 20 Nonlinear transient simulation: journal surface peak-peak ΔT at 8000 and 8500 rpm (with and without TB effect)

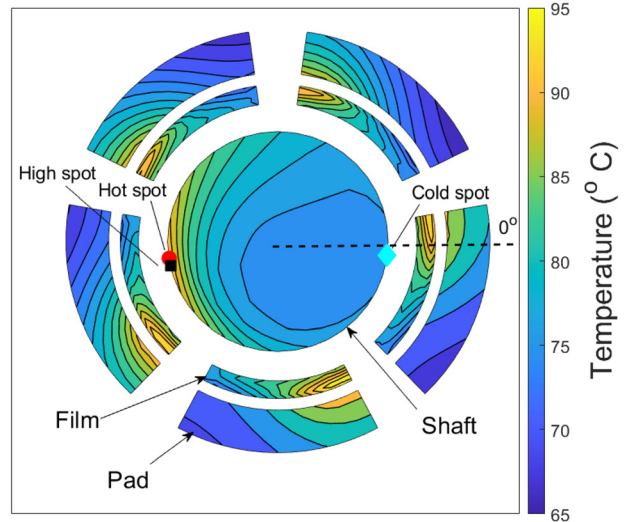


Fig. 21 Nonlinear transient simulation: temperature distribution at bearing midplane of the with TB case at 8500 rpm after 25 min

cage stiffness values. This result confirms that high cage stiffness of the SFD causes increased ME-induced vibration in the example presented. Note that in the linear and nonlinear analysis results in Figs. 12 and 13, the vibration amplitudes at journal location have been reduced with stiffness cage and thus resulting in less journal ΔT .

The higher vibration level with stiffer cage may be due to the decreased effective damping with increasing cage stiffness of bearing support as demonstrated in Ref. [37]. Based on the nonlinear simulations, the cage stiffness value of 1×10^8 N/m, ensures a low journal eccentricity (<0.2) and small vibration amplitudes. This value is selected for the SFD design and will be used for the simulations in the following discussion [35,36].

Simulations are performed with varying levels of SFD force, from 0% to 100% of the nominal value, to demonstrate that the full SFD force is not required to suppress the ME. The cage stiffness of 1×10^8 N/m and the rotor-bearing-SFD parameters in Table 2 are employed for simulation. Figure 26 depicts the nonlinear steady-state result from 3000 rpm to 10,000 rpm. When no SFD force (0% of SFD force) and only cage stiffness are included in the simulation, a much larger vibration amplitude ($42.39 \mu\text{m}$)

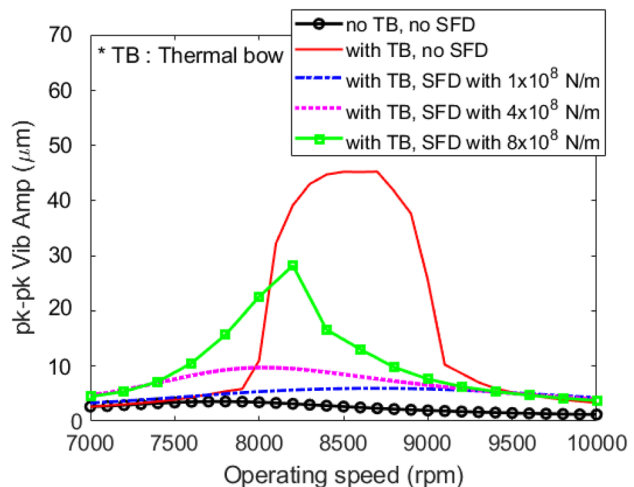


Fig. 22 Nonlinear steady-state simulation: pk-pk vibration amplitude versus rpm at bearing node with different cage stiffness

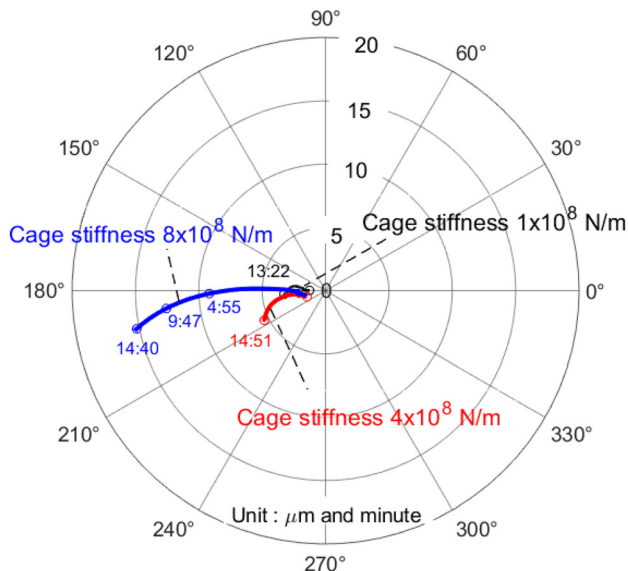


Fig. 23 Nonlinear transient simulation: 1 × polar plot at critical speed with different cage stiffness

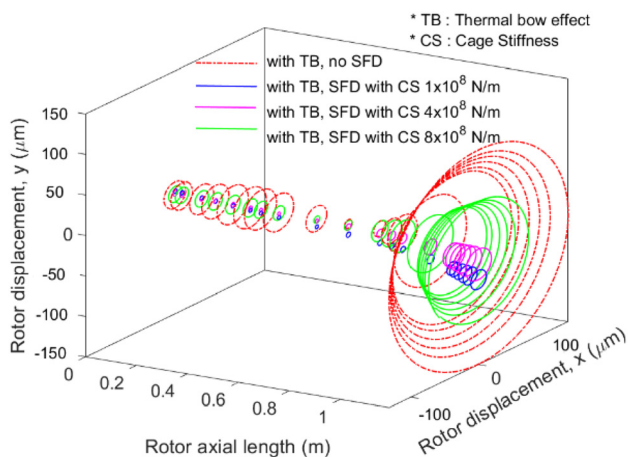


Fig. 24 Nonlinear transient simulation: 3D orbit shapes at critical speed after 25 min with different cage stiffness

than the no TB case occurs at 5000 rpm, indicating ME occurrence. By increasing the SFD force from 10% up to 100% of the nominal value, the high vibration level is mitigated compared with 0% case. Note that the most stable vibration with the smallest pk–pk vibration at its resonance speed occurs with 50% of SFD force, which confirms the existence of optimal damping in terms of vibration suppression [20]. The linear analysis in Figs. 14–16 also indicated the existence of optimal SFD parameters, which showed more improved stability of the rotor. The relocation of the critical speed is also observed with the SFD force variation. With the 0% SFD force and with the cage stiffness, the critical speed at the low speed of 5000 rpm appears while the counterpart of no SFD case is around 7600 rpm. By increasing the ratio of the SFD force, the critical speed shifts up to its maximum value of 8500 rpm with 100% of the nominal force. The result confirms that the cage stiffness alone is not effective in controlling the ME vibration, and the damping force from the SFD is needed to suppress the ME.

Comparison Between With and Without Squeeze Film Damper. Figure 27(a) depicts the pk–pk vibration of the bearing with time at the speed where maximum vibration level appears in

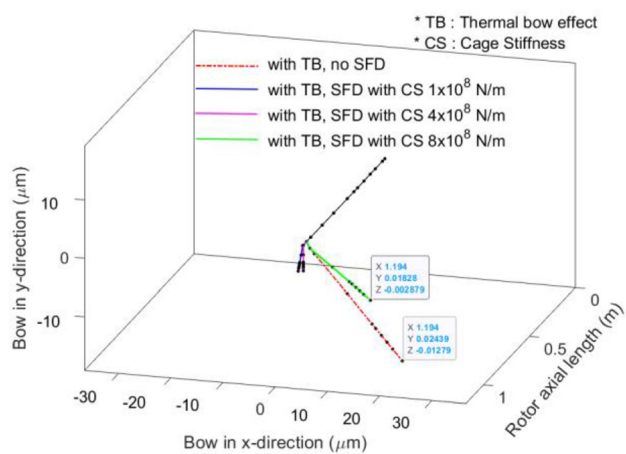


Fig. 25 Nonlinear transient simulation: TB of shaft at critical speed after 25 min with different cage stiffness

nonlinear simulation. Three different cases are considered, i.e., case 1: no thermal bow and no SFD (TPJB rigidly mounted), case 2: with thermal bow and no SFD, case 3: with thermal bow and SFD (cage stiffness of 1×10^8 N/m). In case 3, the high vibration induced by the ME is suppressed to an acceptable level, but the vibration level is still higher than case 1. In Fig. 27(b), the magnitude of the SFD damping and inertia forces from case 2 increase with time and converge to 1076 N and 68 N, respectively.

The migration of the hot spot on the journal surface causes the phase-varying thermal bow and thus the varying phase in the induced ME vibration. In the process, the hot spot typically lags the high spot (minimum film thickness) on the journal due to the convection effect in the lubricant film. Therefore, the occurrence of the ME is closely related to the stability of the hot spot. It is known that when the ME occurs, the hot spot moves around the journal circumference, and the phase lag between hot and high spots changes accordingly [1,2]. In this regard, the phase lag between high and hot spots at various operating speeds are investigated. The phase lag values are measured after 25 min via nonlinear simulation in Table 3. The comparison between cases 1 and 2 reveals that phase lags are similar regardless of the thermal bow inclusion at the speeds where the ME induced vibration is not evident, as shown in Fig. 17 (7500, 9000, and 9500 rpm). At 8000 rpm, the ME starts to influence the rotor vibration in Fig. 17, and the phase lag changes from 0 deg to 360 deg during most of the simulation, and eventually converges to 8.23 deg, which is similar to that of case 1.

At 8500 rpm, the thermal spiral is nonconverging type, and the rotor exhibits the high vibration with varying phase until 25 min. The corresponding hot spot location with time is shown in Fig. 28. The angle shown in the figure provides the angular position of the hot spot relative to the angular position of the original imbalance, which is fixed at 0 deg, and this is shown in Fig. 21.

The hot spot angle of case 2 keeps varying in a wide range and does not converge to a steady-state value, while those of cases 1 and 3 show stable and converging angles with time. Note that case 3 shows relatively increased and stable phase lags ranging from 10.8 deg to 12.32 deg compared with two other cases without the SFD. The stable hot spot angles and increased phase lag may explain the enhanced stability and the ME suppression in the rotor-bearing due to the SFD.

Figure 29 illustrates the temperature distribution at the bearing midplane of case 3 after 25 min of simulation at its critical speed (8600 rpm), where the high spot leads the hot spot with 11.72 deg. Comparing with that of case 2 at the same instance in Fig. 21 reveals that the induced high ΔT is suppressed in case 3 as displayed by the concentric distribution of the journal temperature. This may be attributed to the addition of the SFD, which reduced

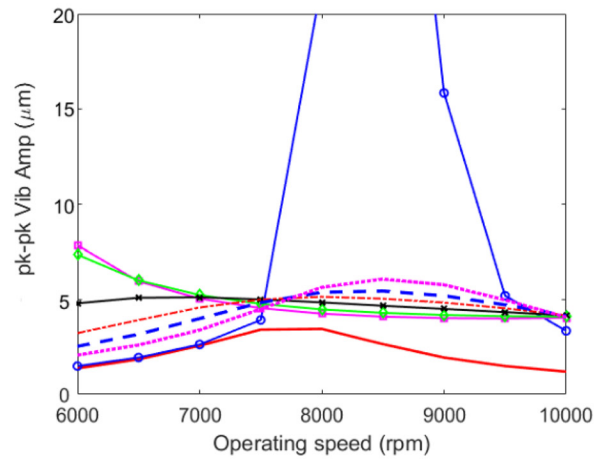
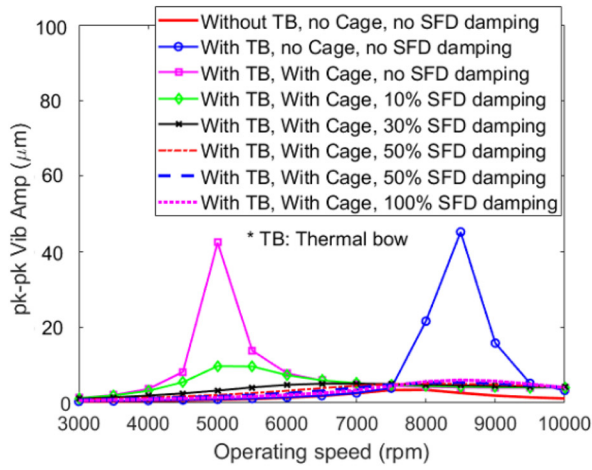


Fig. 26 Nonlinear transient simulation: (a) pk-pk vibration amplitude versus rpm at bearing node at critical speed after 25 min (b) zoom of (a)

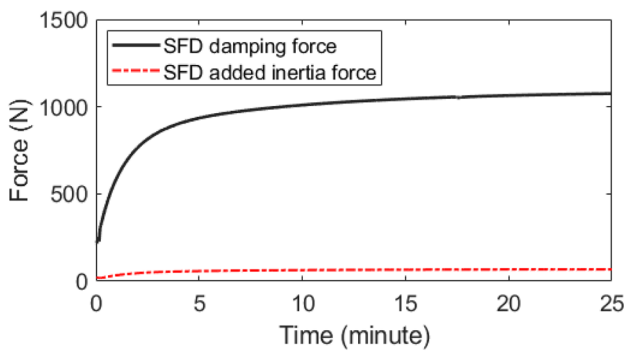
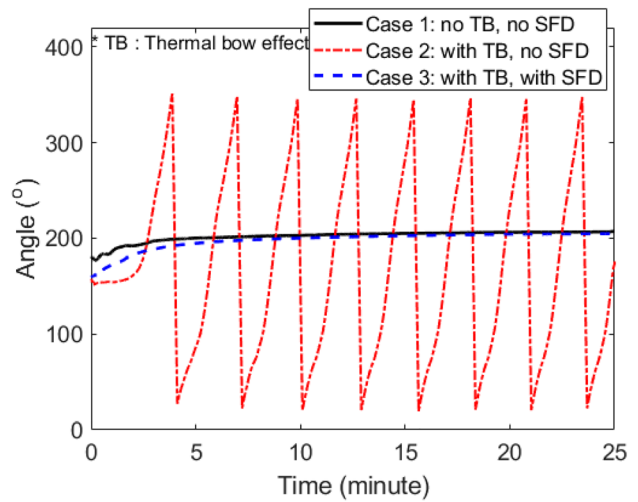
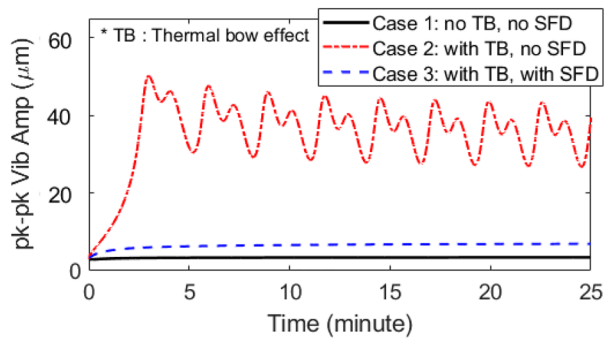


Fig. 28 Nonlinear transient simulation: hot spot location change with time at critical speed (no SFD indicates rigidly mounted TPJB)

Fig. 27 Nonlinear transient simulation: (a) pk-pk vibration amplitude and (b) SFD damping and added inertia force from case 3 at critical speed

Table 3 Phase lag between high and hot spots (case 1: no TB and no SFD, case 2: with TB and no SFD, case 3: with TB and with SFD)

	7500 rpm	8000 rpm	8500 rpm	9000 rpm	9500 rpm
Case 1	6.93 deg	8.49 deg	9.39 deg	6.998 deg	3.633 deg
Case 2	6.66 deg	8.23 deg	NC	7.173 deg	3.641 deg
Case 3	12.32 deg	11.83 deg	11.23 deg	11.72 deg	10.8 deg

NC, nonconverging.

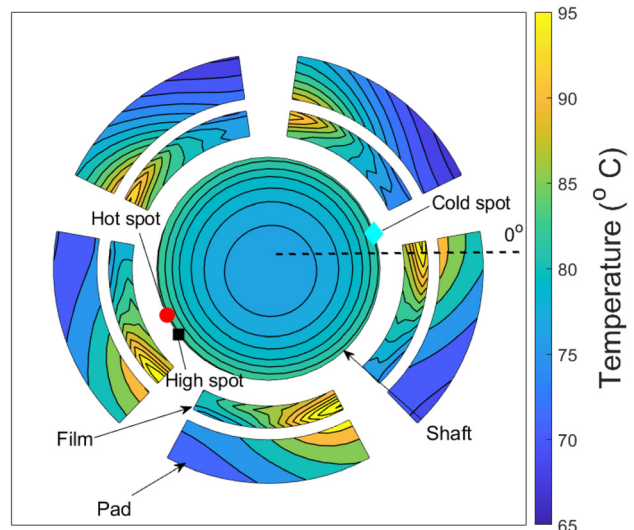


Fig. 29 Nonlinear transient simulation: temperature distribution at bearing midplane at 25 min with SFD

the vibration amplitudes at the journal location as demonstrated from the linear unbalance analysis in Fig. 12. The reduced synchronous orbits within the journal may result in less asymmetric heating of the journal as evidenced in Fig. 13.

Conclusion

The mitigation of the ME-induced vibration utilizing a squeeze film damper with a central groove has been presented. Three-dimensional FEM based rotordynamic and thermodynamic models of the ME were utilized. The ME model was benchmarked with an experimental result, and similar trends of spiral vibration were observed. However, the ME speed range and predicted vibration amplitudes depart from the experimental case under some conditions, due to unmodeled effects. The following conclusions are made based on convectional linear analysis and nonlinear transient ME simulations: (1) based on conventional rotordynamic linear analysis, the SFD in series with the TPJB shifts the first forward critical speed of the overhung rotor. Mounting the SFD with low stiffness could raise the rotor's critical speed above the original one without SFD. However, this positive shift of critical speed could be unfavorably reduced if an improper SFD with a much higher stiffness is chosen. (2) The SFD with adequately designed parameters suppresses the ME-induced vibration. The cage stiffness of the SFD significantly affects the ME suppression capability of the SFD. In the current rotor-bearing-SFD case, a stiffer cage induces larger vibration at journal location in the linear unbalance response, which may cause increased viscous heating in a journal circumference and consequently more severe ME vibration in the nonlinear simulations. A cage stiffness of 1×10^8 N/m was shown to be optimal for suppressing the ME, compared with two other cases 4×10^8 N/m and 8×10^8 N/m, for the particular rotor model presented. This may of course vary between machines considered. For comparison, the optimal cage stiffness was 25% of the average x and y linear bearing stiffness values. (3) The installation of the cage stiffness without the SFD damping force was unable to control the ME vibration. The damping force from the SFD, along with the cage, increased the critical speed and suppressed the ME. (4) There exist optimal parameters for the SFD that offer the best suppression of the ME, and this is verified via the nonlinear ME simulations. Future work will include experimental verification of the ME suppression using the SFD with a central groove. SFD lubricant temperature variation and thermal conduction effect through SFD/TPJB housings will be considered in future work. In addition, an advanced optimization technique will be applied for the optimal SFD parameter identification to suppress the ME.

Acknowledgment

The authors gratefully acknowledge support of this research from the Texas A&M Turbomachinery Research Consortium (TRC) members companies.

Nomenclature

c = TPJB lubricant's specific heat capacity
 C_b = TPJB bearing clearance
 C_D = SFD radial clearance
 C_P = TPJB pad clearance
 C_{ro} = damping matrix of Euler beam rotor
CS = cage spring
 d_l = SFD inlet groove depth
 \hat{e}_x = TPJB journal displacement in x direction
 \hat{e}_y = TPJB journal displacement in y direction
 $F_{B,x,y}$ = sum of TPJB pads' force
 $F_{D,x,y}$ = SFD damping force
 F_{pad}^i = fluid film force acting on pads
 $F_{SFD,x,y}$ = SFD force in x and y direction
 h = TPJB film thickness

h_D = SFD film thickness
 $h_{pad,TE}$ = thermal expansion of TPJB pads
 $h_{shaft,TE}$ = thermal expansion of TPJB shaft
 I_{tilt}^i = pad inertia of TPJB
 k = TPJB lubricant's thermal conductivity
 K_{Dx} = SFD cage spring stiffness in x direction
 K_{Dy} = SFD cage spring stiffness in y direction
 K_p = pad pivot stiffness
 K_{ro} = stiffness matrix of Euler beam rotor
 M_D = TPJB housing mass
 $M_{D,x,y}$ = SFD added inertia force
 M_{pad}^i = pad mass of TPJB
 M_{ro} = Maxx matrix of Euler beam rotor
ME = Morton effect
 O_D = SFD journal center
 R = TPJB journal radius
 R_J = TPJB housing radius
 y_{pvt} = pivot displacement of TPJB
 N_{tilt}^i = fluid film tilting moment acting on pads
SFD = squeeze film damper
TB = thermal bow
TPJB = tilting pad journal bearing
 u = lubricant's circumferential fluid velocity
 U = state variable vector of Euler beam rotor
 x_{JD} = SFD journal displacement in x direction
 y_{JD} = SFD journal displacement in y direction
 z = axial coordinate of TPJB film
 z_D = axial coordinate of SFD film
 δ_{tilt} = tilting angle of TPJB pads
 μ_D = SFD lubricant viscosity
 θ = circumferential coordinate of TPJB film
 θ_D = circumferential coordinate of SFD film
 θ_p = pad pivot's circumferential location
 ρ = TPJB lubricant's density
 ρ_D = SFD lubricant density
 ω_J = SFD journal rotating speed

References

- [1] Tong, X., Palazzolo, A., and Suh, J., 2017, "A Review of the Rotordynamic Thermally Induced Synchronous Instability (Morton) Effect," *ASME. Appl. Mech. Rev.*, **69**(6), p. 060801.
- [2] de Jongh, F., 2008, "The Synchronous Rotor Instability Phenomenon—Morton Effect," *37th Turbomachinery Symposium*, Houston, TX, Sept. 8–11, pp. 159–167.
- [3] 1998, "Application of a Heat Barrier Sleeve to Prevent Synchronous Rotor Instability," *27th Turbomachinery Symposium*, F. de Jongh, and P. Van Der Hoeven, eds., Houston, TX, Sept. 20–24, pp. 17–26.
- [4] Keogh, P., and Morton, P., 1994, "The Dynamic Nature of Rotor Thermal Bending Due to Unsteady Lubricant Shearing Within a Bearing," *Proc. R. Soc. London, Ser. A*, **445**(1924), pp. 273–290.
- [5] Lee, J. G., and Palazzolo, A., 2012, "Morton Effect Cyclic Vibration Amplitude Determination for Tilt Pad Bearing Supported Machinery," *ASME. J. Tribol.*, **135**(1), p. 011701.
- [6] Suh, J., and Palazzolo, A., 2015, "Three-Dimensional Dynamic Model of TEHD Tilting-Pad Journal Bearing—Part I: Theoretical Modeling," *ASME. J. Tribol.*, **137**(4), p. 041703.
- [7] Suh, J., and Palazzolo, A., 2015, "Three-Dimensional Dynamic Model of TEHD Tilting-Pad Journal Bearing—Part II: Parametric Studies," *ASME. J. Tribol.*, **137**(4), p. 041704.
- [8] Suh, J., and Palazzolo, A., 2014, "Three-Dimensional Thermohydrodynamic Morton Effect Simulation—Part I: Theoretical Model," *ASME. J. Tribol.*, **136**(3), p. 031706.
- [9] Suh, J., and Palazzolo, A., 2014, "Three-Dimensional Thermohydrodynamic Morton Effect Analysis—Part II: Parametric Studies," *ASME. J. Tribol.*, **136**(3), p. 31707.
- [10] Tong, X., Palazzolo, A., and Suh, J., 2016, "Rotordynamic Morton Effect Simulation With Transient, Thermal Shaft Bow," *ASME. J. Tribol.*, **138**(3), p. 031705.
- [11] Tong, X., and Palazzolo, A., 2016, "Double Overhung Disk and Parameter Effect on Rotordynamic Synchronous Instability—Morton Effect—Part I: Theory and Modeling Approach," *ASME. J. Tribol.*, **139**(1), p. 011705.
- [12] Tong, X., and Palazzolo, A., 2016, "Double Overhung Disk and Parameter Effect on Rotordynamic Synchronous Instability—Morton Effect—Part II: Occurrence and Prevention," *ASME. J. Tribol.*, **139**(1), p. 011706.
- [13] Tong, X., and Palazzolo, A., 2018, "Tilting Pad Gas Bearing Induced Thermal Bowrotor Instability," *Tribol. Int.*, **121**, pp. 269–279.

- [14] Tong, X., and Palazzolo, A., 2017, "Measurement and Prediction of the Journal Circumferential Temperature Distribution for the Rotordynamic Morton Effect," *ASME J. Tribol.*, **140**(3), p. 031702.
- [15] Leader, M. E., Whalen, J. K., and Grey, G. G., 1995, "The Design and Application of a Squeeze Film Damper Bearing to a Flexible Steam Turbine Rotor," *24th Turbomachinery Symposium*, College Station, TX, Sept. 25–28, pp. 49–58.
- [16] Edney, S. L., and Nicholas, J. C., 1999, "Retrofitting a Large Steam Turbine With a Mechanically Centered Squeeze Film Damper," *27th Turbomachinery Symposium*, Houston, TX, Sept. 20–24, pp. 29–40.
- [17] Kanki, H., Kaneko, Y., Kurosawa, M., and Yamamoto, T., 1998, "Prevention of Low-Frequency Vibration of High-Capacity Steam Turbine Units by Squeeze-Film Damper," *ASME J. Eng. Gas Turbines Power*, **120**(2), pp. 391–396.
- [18] Ferraro, R., Catanzaro, M., Kim, J., Massini, M., and Betti, D., 2016, "Suppression of Subsynchronous Vibrations in a 11 MW Steam Turbine Using Integral Squeeze Film Damper Technology at the Exhaust Side Bearing," *ASME Paper No. GT2016-57410*.
- [19] Ertas, B., Cerny, V., Kim, J., and Polreich, V., 2015, "Stabilizing a 46 MW Multistage Utility Steam Turbine Using Integral Squeeze Film Bearing Support Dampers," *ASME J. Eng. Gas Turbines Power*, **137**(5), p. 52506.
- [20] Barrett, L. E., Gunter, E. J., and Allaire, P. E., 1978, "Optimum Bearing and Support Damping for Unbalance Response and Stability of Rotating Machinery," *ASME J. Eng. Power*, **100**(1), pp. 89–94.
- [21] Chu, F., and Holmes, R., 2000, "The Damping Capacity of the Squeeze Film Damper in Suppressing Vibration of a Rotating Assembly," *Tribol. Int.*, **33**(2), pp. 81–97.
- [22] San Andres, L., and Vance, J., 1987, "Experimental Measurement of the Dynamic Pressure Distribution in a Squeeze-Film Bearing Damper Executing Circular Centered Orbits," *ASLE Trans.*, **30**(3), pp. 373–383.
- [23] Lund, J. W., Myllerup, C. M., and Hartmann, H., 2003, "Inertia Effects in Squeeze-Film Damper Bearings Generated by Circumferential Oil Supply Groove," *ASME J. Vib. Acoust. October*, **125**(4), pp. 495–499.
- [24] Kim, K., and Lee, C., 2005, "Dynamic Characteristics of Sealed Squeeze Film Damper With a Central Feeding Groove," *ASME J. Tribol.*, **127**(1), pp. 103–111.
- [25] San Andrés, L., 2012, "Damping and Inertia Coefficients for Two Open Ends Squeeze Film Dampers With a Central Groove: Measurements and Predictions," *ASME J. Eng. Gas Turbines Power*, **134**(10), p. 102506.
- [26] San Andrés, L., and Seshagiri, S., 2013, "Damping and Inertia Coefficients for Two End Sealed Squeeze Film Dampers With a Central Groove: Measurements and Predictions," *ASME J. Eng. Gas Turbines Power. November*, **135**(11), p. 112503.
- [27] San Andrés, L., 2014, "Force Coefficients for a Large Clearance Open Ends Squeeze Film Damper With a Central Feed Groove: Experiments and Predictions," *Tribol. Int.*, **71**, pp. 17–25.
- [28] San Andrés, L., and Jeung, S., (October 7, 2014), "Experimental Performance of an Open Ends, Centrally Grooved, Squeeze Film Damper Operating With Large Amplitude Orbital Motions," *ASME J. Eng. Gas Turbines Power*, **137**(3), p. 032508.
- [29] Delgado, A., and San Andrés, L., 2010, "A Model for Improved Prediction of Force Coefficients in Grooved Squeeze Film Dampers and Oil Seal Rings," *ASME J. Tribol.*, **132**(3), p. 032202.
- [30] Andrés, L. S., and Delgado, A., 2012, "A Novel Bulk-Flow Model for Improved Predictions of Force Coefficients in Grooved Oil Seals Operating Eccentrically," *ASME J. Eng. Gas Turbines Power*, **134**(5), p. 052509.
- [31] Bonello, P., Brennan, M. J., and Holmes, R., 2004, "A Study of the Nonlinear Interaction Between an Eccentric Squeeze Film Damper and an Unbalanced Flexible Rotor," *ASME J. Eng. Gas Turbines Power*, **126**(4), pp. 855–866.
- [32] He, F., 2013, "Forced Response With Stability of Flexible Rotor-Bearing Systems With Squeeze Film Dampers," *Ph.D. thesis*, University of Virginia, Charlottesville, VA.
- [33] Cao, J., Allaire, P., and Dimond, T., 2015, "Coupled Lateral and Torsional Non-linear Transient Rotor-Bearing System Analysis With Applications," *ASME J. Dyn. Sys., Meas., Control*, **137**(9), p. 091011.
- [34] Kang, X., 2019, "Simulation and Test of the Auxiliary Bearings and Their Dampers in Magnetic Bearing Systems," *Ph.D. dissertation*, Texas A&M University, College Station, TX.
- [35] Zeidan, F., San Andres, L., and Vance, J., 1996, "Design and Application of Squeeze Film Dampers in Rotating Machinery," *25th Turbomachinery Symposium*, College Station, TX, Sept. 17–19, pp. 169–188.
- [36] Shin, D., and Palazzolo, A. B., 2020, "Tilting Pad Journal Bearing Misalignment Effect on Thermally Induced Synchronous Instability (Morton Effect)," *ASME J. Tribol.*, **143**(3), p. 031802.
- [37] Shin, D., Yang, J., Tong, X., Suh, J., and Palazzolo, A., 2020, "A Review of Journal Bearing Thermal Effects on Rotordynamic Response," *ASME J. Tribol.*, **143**(3), p. 031803.